Science Advances
AAAS

advances.sciencemag.org/cgi/content/full/6/43/eabb7438/DC1

Supplementary Materials for

Versatile phenotype-activated cell sorting

Jihwan Lee, Zhuohe Liu, Peter H. Suzuki, John F. Ahrens, Shujuan Lai, Xiaoyu Lu, Sihui Guan, François St-Pierre*

*Corresponding author. Email: stpierre@bcm.edu

Published 23 October 2020, *Sci. Adv.* **6**, eabb7438 (2020)
DOI: 10.1126/sciadv.abb7438

The PDF file includes:

Other Supplementary Material for this manuscript includes the following:

(available at advances.sciencemag.org/cgi/content/full/6/43/eabb7438/DC1)

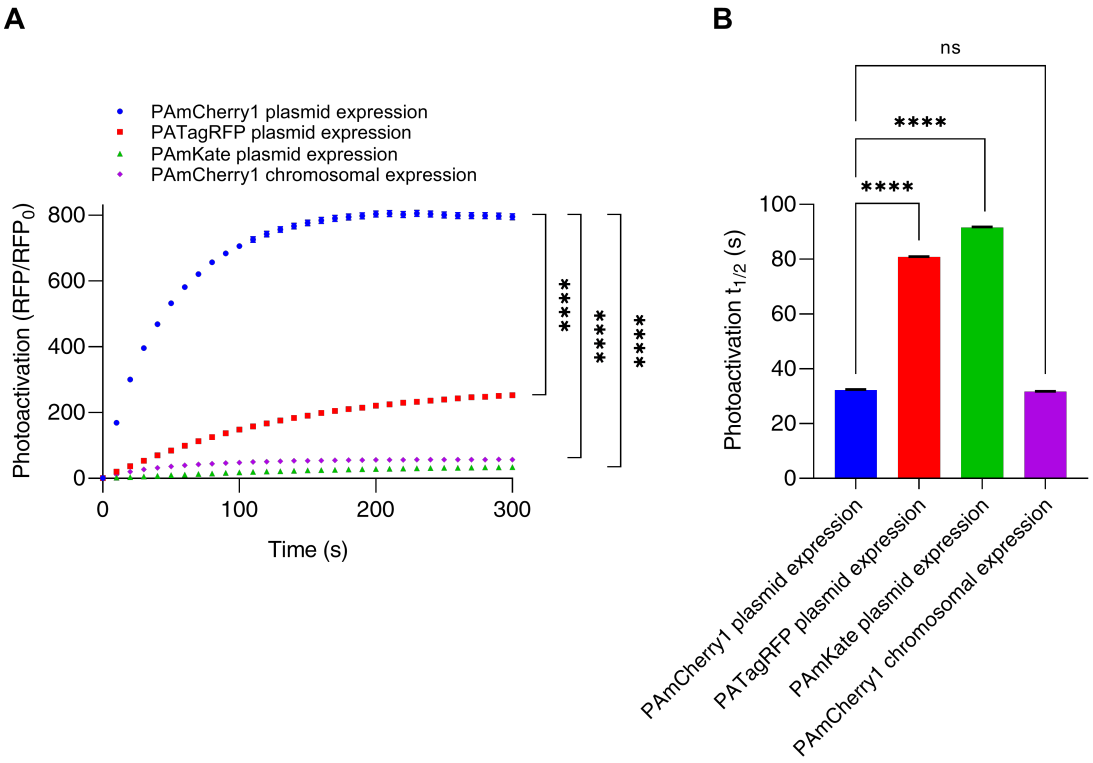

Fig. S1. PAmCherry1 produced larger and faster intensity changes than other PA-RFPs in yeast cells. (**A**) Photoactivation contrast ratio of three different PA-RFPs constitutively expressed from a multi-copy 2-micron plasmid or from the genome. RFP_0 is the red fluorescence at t = 0 s. For each PA-RFP, a field-of-view containing 6,000 to 8,000 cells were simultaneously photoactivated by continuously shining 410/20-nm light at 11.4 mW/mm^2 for 5 min. RFP intensity was monitored every 10 s during photoactivation. Data points correspond to the mean and the error bars represent the SEM. $p \leq 0.0001$, Welch's ANOVA test comparing the areas under the curves of individual cells expressing different PA-RFPs. ****, $p \leq 0.0001$ for *post-hoc* tests (Games-Howell's multiple comparison test). (**B**) Comparison of photoactivation kinetics. Using the same data as in (A), the time to reach half of the maximum photoactivation contrast ratio (photoactivation $t_{1/2}$) was calculated for each cell. Mean values from 6,000 to 8,000 cells are shown. The error bars represent SEM. $p \leq 0.0001$, Welch's ANOVA test. ****, $p \leq 0.0001$; 'ns', not significant for the *post-hoc* test (Games-Howell's multiple comparison test).

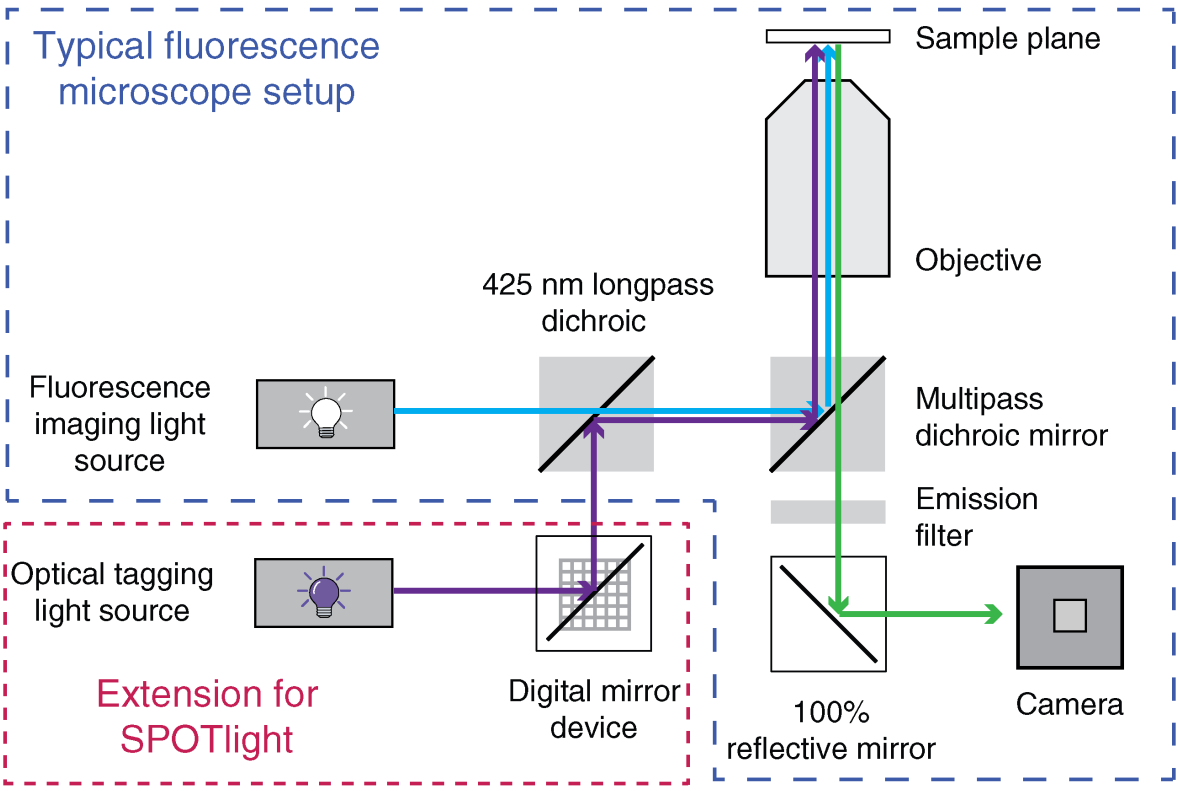

Fig. S2. Schematic of the optical train of our instantiation of the SPOTlight platform. The collimated beam (purple arrows) of an 410/20-nm light source (UHP-F5-405, Prizmatix) is spatially patterned by a digital mirror device (TI-LA-DMD, Nikon Instruments) to selectively illuminate and optically tag target cells. Imaging light with wavelengths > 425 nm (SpectraX, Lumencor) is combined with the violet optical tagging light using a 2-mm-thick 425-nm long-pass dichroic mirror (T425lpxr-UF2, Chroma). Excitation light (blue arrows) is reflected by a multiplass dichroic mirror and focused onto the sample by an objective. Light emitted from the sample (green arrows) is collected by the objective, transmitted through the multipass dichroic mirror, filtered by a multipass emission filter, and imaged using a camera. See Methods for further details on components and procedures.

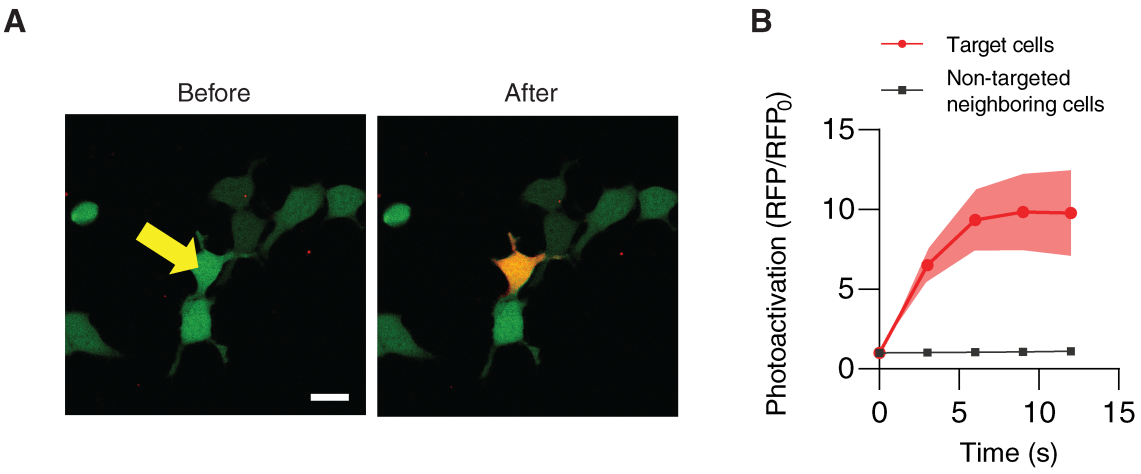

Fig. S3. Two-photon laser scanning microscopy can be used to optically tag single cells. (**A-B**) Human cells (HEK239A) were co-transfected with EGFP and PAmCherry1 expression plasmids. Target cells were selectively photoactivated by scanning a two-photon laser beam at 800 nm. (**A**) Photoactivation of a representative target cell (yellow arrow). Images show the overlay of green and red fluorescence images. Scale bar, 20 μm. (**B**) Optical tagging was specific to the target cells, with negligible activation of neighboring cells. Data points represent the mean photoactivation contrast ratio of 8 cells/group. The shaded regions represent SEM.

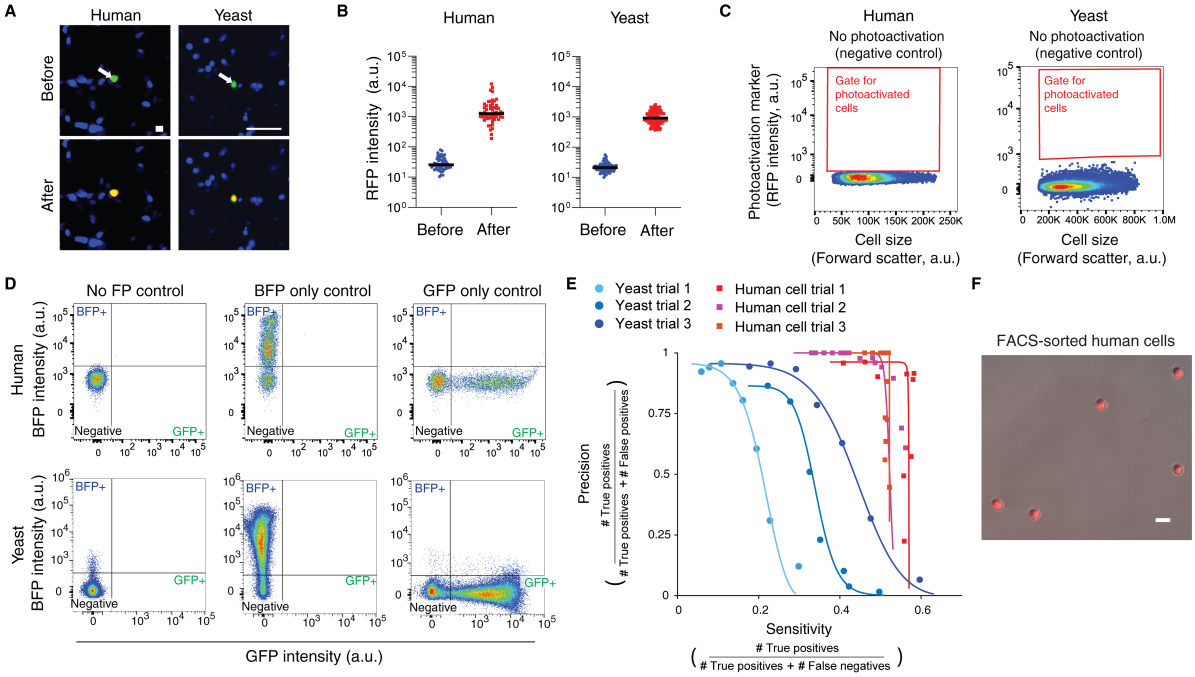

Fig. S4. Quantifying the sensitivity and precision of SPOTlight on human or yeast cells. (A-D) Imaging and gating controls of single-cell optical tagging and retrieval (**Fig. 2**). (**A**) Single-cell photoactivation of a representative GFP+ human cell (*left*) and yeast cell (*right*). Arrows point to the target cells. Cells were selectively photoactivated using a 230 μm^2 (human) or 4 μm^2 (yeast) spot of light. Overlays of RFP, GFP, and BFP channels are shown. Scale bars, 20 µm. (**B**) Mean RFP intensities of the 56 photoactivated human cells and 96 photoactivated yeast cells before and after photoactivation. The black lines indicate the median values. Photoactivation increased RFP intensity by ~50-60-fold for both human and yeast cells. Note that photoactivation contrast ratio was smaller than that in Fig. 2B because a smaller photoactivation spot size was used in this experiment. The error bars indicate the SEM. (**C**) The boundaries of the photoactivated gate were determined using a negative control with no photoactivated cells. (**D**) GFP+ and BFP+ gates were determined using cells with an empty plasmid (*left*), a BFP-expressing plasmid (*middle*) or a GFP-expressing plasmid. *Top row*, human cells. *Bottom row,* yeast cells. (**E**) The gating strategy for photoactivated cells (i.e. RFP+ cells) changes the sensitivity and precision of SPOTlight. Flow cytometry data of the experiment described in Fig. 2 and two additional repeats were used to determine the sensitivity and precision when the photoactivated cell gate was located closer to or further away from the non-photoactivated population of cells (i.e. decrease or increase the RFP intensity threshold to define photoactivated cells). The circle (yeast trials) and square (human cell trials) markers represent the sensitivity and precision at various RFP intensity thresholds. The solid lines represent best-fit lines computed by simulating the recovery of photoactivated cells. (**F**) A representative field-of-view of photoactivated HEK239A cells imaged after FACS. Scale bar, 20 µm. Optical tagging and recovery was conducted as described in Fig. 3A-C.

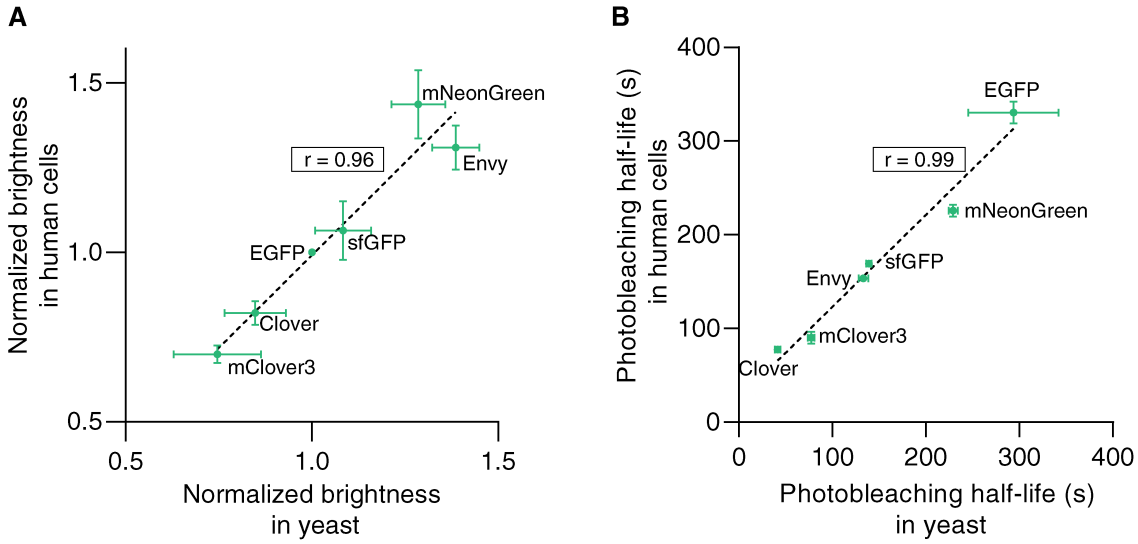

Fig. S5. Fluorescent protein brightness and photostability in yeast and human cells are correlated when yeast cells are grown at 37°C and pH 7.0. (**A-B**) Yeast or human cells (HEK293A) harboring plasmids expressing one of six commonly used GFPs and their brightness (A) and photostability (B) were quantified. (**A**) Relative brightness of GFPs in yeast and human cells is highly correlated. Brightness under 470/24-nm light was quantified in individual cells. The red fluorescent protein mCherry, expressed from the same plasmid as the GFPs, was used to normalize for differences in copy number or expression capacity. Data points are the mean values, normalized to the brightness of EGFP for three independent yeast cultures (> 5,000 cells analyzed per culture) or three independent transfections (> 50-200 cells analyzed per transfection) The error bars correspond to the SEM. The black dotted line corresponds to the linear regression. r, Pearson correlation coefficient. (**B**) Relative photostability of GFPs in yeast and human cells is highly correlated. Photostability was quantified by taking images of the cells prepared in (A) with 10 s intervals during 7 min of continuous widefield illumination with 470/24-nm light at 40.7 mW/mm^2. Datapoints are the mean of three independent yeast cultures (> 5,000 analyzed cells per culture) or human cell transfections (> 50 cells/transfection). The error bars correspond to the SEM. The black dotted line corresponds to the linear regression. r, Pearson correlation coefficient.

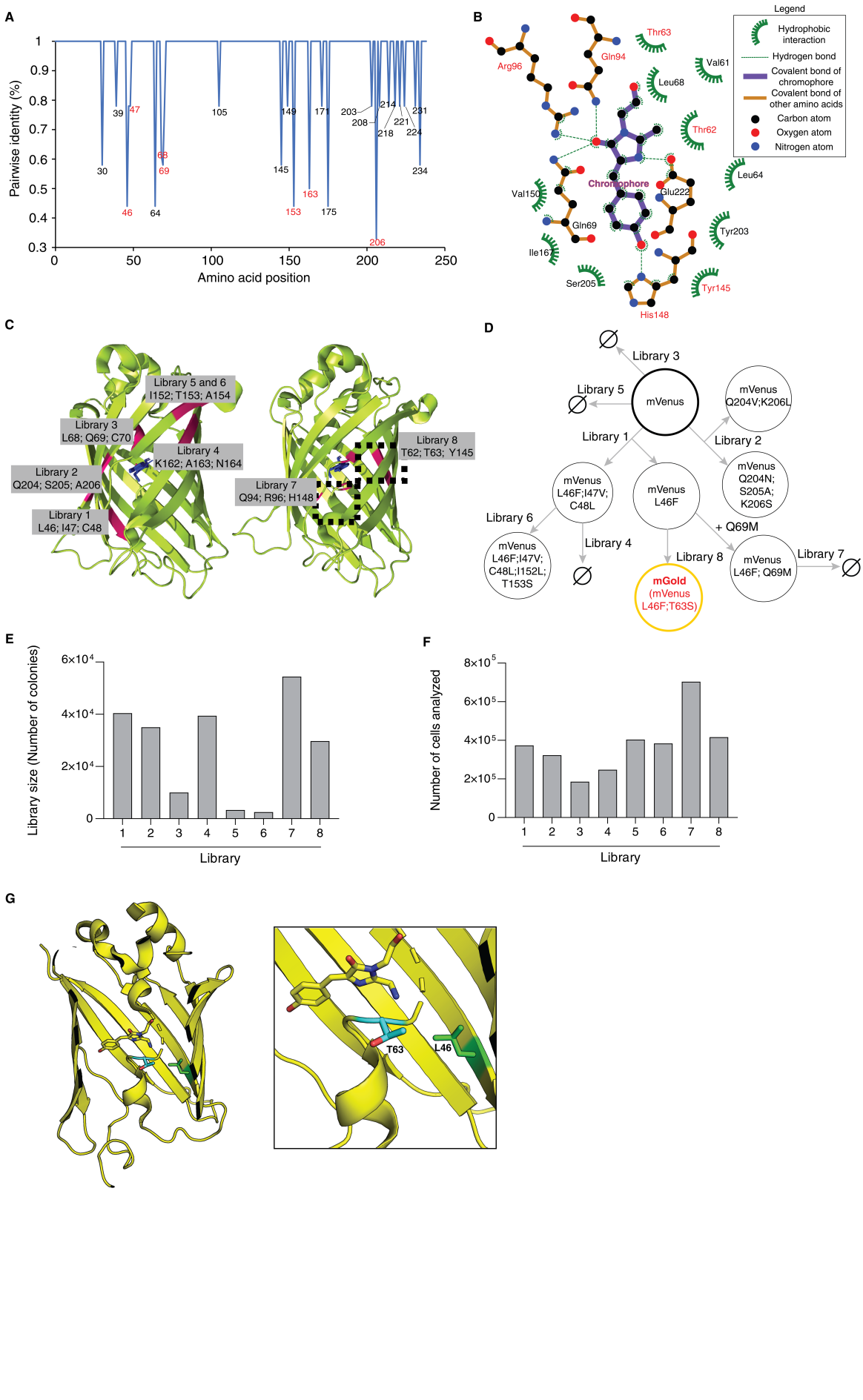
A
Pairwise identity (%)
Amino acid position
B
Legend
Hydrophobic interaction
Hydrogen bond
Covalent bond of chromophore
Covalent bond of other amino acids
Carbon atom
Oxygen atom
Nitrogen atom
Chromophore
C
Library 5 and 6
I152; T153; A154
Library 3
L68; Q69; C70
Library 4
K162; A163; N164
Library 2
Q204; S205; A206
Library 1
L46; I47; C48
Library 8
T62; T63; Y145
Library 7
Q94; R96; H148
D
Library 3
Library 5
mVenus
mVenus Q204V;K206L
Library 1
Library 2
mVenus L46F;I47V; C48L
mVenus L46F
mVenus Q204N; S205A; K206S
Library 6
+ Q69M
Library 4
Library 8
Library 7
mVenus L46F;I47V; C48L;I152L; T153S
mGold (mVenus L46F;T63S)
mVenus L46F; Q69M
E
Library size (Number of colonies)
Library
F
Number of cells analyzed
Library
G
T63
L46

Fig. S6. Summary of fluorescent protein mutagenesis and screening. (A,B) Selecting mVenus residues for mutagenesis. (**A**) Residues that show large variations between engineered YFPs were selected for mutagenesis. First, protein sequences of 9 YFPs (mVenus, Venus, SYFP2, moxVenus, SHardonnay, EYFP, mCitrine, and Citrine2) were aligned using global alignment with free end gaps and the Blosum62 scoring matrix (*66*). The pairwise identity percentage was then computed by dividing the number of identical pairs by the total number of pairs. The numbers below the peaks correspond to the position of residues with low pairwise identity and red font was used to denote the residues mutated in this study. Several chosen residues were prioritized due to ease of cloning (e.g. mutations located close by can be easily combined on the same primer). (**B**) Chromophore-interacting residues were selected for mutagenesis. LigPlot+ was used to identify residues making hydrophobic or hydrogen bond interactions with the chromophore using the crystal structure of Venus (PDB: 1MYW). The amino acids labeled in red were mutagenized in this study. Several chosen residues were prioritized due to ease of cloning (e.g. mutations located close by can be easily combined on the same primer). Note that residue Y203 constitutes the chromophore. However, Y203 was not defined as the chromophore in this analysis because the LigPlot+ software only allows covalently linked structures as a chromophore and Y203 is not covalently linked to the rest of the chromophore. **(C-D)** Summary of screening results conducted in this study. (**C**) Location of mutagenesis sites (in pink) on the 3-dimensional crystal structure of Venus (PDB:1MYW). Libraries 1 to 8 are color-coded and the amino acid types and positions are indicated. (**D**) Graphical depiction of the relationship between the libraries. The nodes are the best variants selected from the libraries, and the edges are the libraries denoted in panel (a). The fast-maturing Q69M mutation (*28*) was directly introduced to mVenus(L46F), and the outcome mVenus(L46F;Q69M) was used as a template to construct Library 7. Empty symbols (∅) mean that no improved variant was found. Our most photostable variant mVenus(L46F;T63S) was renamed as mGold, and is shown in red. (**E**) The size of the screened libraries is defined as the total number of colonies on mutagenesis library transformation plates. (**F**) The number of individual cells analyzed during screening. (**G**) *Left,* crystal structure of Venus (PDB:1MYW) highlighting the residues mutated in mGold: L46 (green) and T63 (cyan). *Right*, expanded view of the peri-chromosomal region.

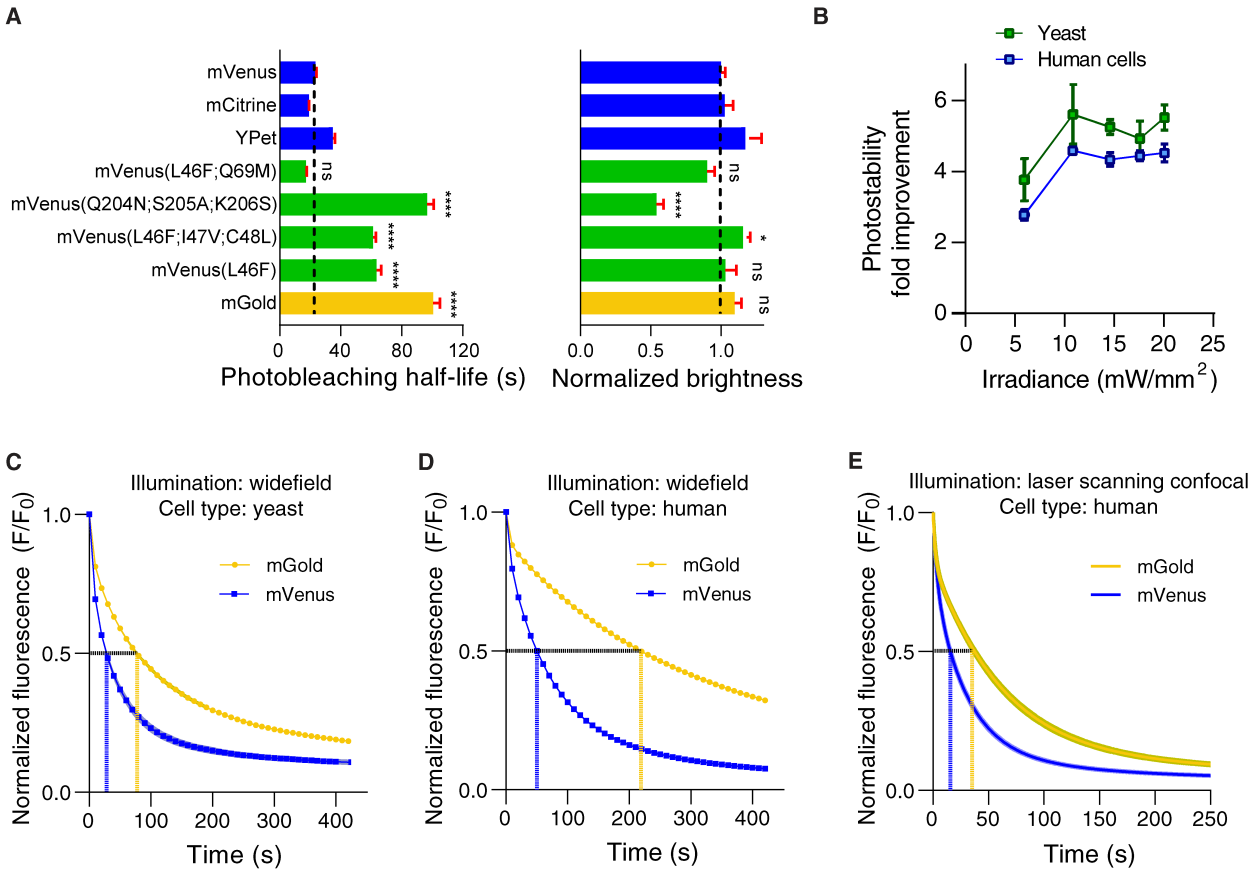

Fig. S7. Comparison of the brightness and photostability of mGold to screening intermediates, mVenus, and other commonly used YFPs. (**A**) Commonly used YFPs (blue bars) and mutagenesis variants (green and yellow bars) were expressed in yeast and photobleached as described in Fig. 4. For each variant, the photobleaching half-lives (*left*) and brightness (*right*) of 2,000-7,000 cells were quantified. A BFP (TagBFP) was co-expressed from the yeast expression vector to normalize for cell-to-cell variation in plasmid copy number and expression capacity; brightness was calculated as the ratio of yellow and blue fluorescence, and normalized to the brightness of mVenus. The data plotted correspond to mean values (n = 3 independent cultures). Error bars indicate the SEM of the triplicates. $p \leq 0.0001$ for one-way ANOVAs for both brightness and photostability. The p values of *post hoc* comparisons with mVenus used the Bonferroni correction for multiple comparisons and are shown on the plot: 'ns', not significant; *, $p \leq 0.05$; ****, $p \leq 0.0001$. (**B**) Photostability fold improvement of mGold compared with mVenus, calculated by dividing the photobleaching half-lives of mGold with those for mVenus in yeast (green markers) and human cells (blue markers) at various irradiances. Photobleaching half-lives are from Fig. 5B. The data points correspond to mean values (n = 3 independent cultures). Error bars indicate the SEM. (**C-E**) Photobleaching dynamics of mGold and mVenus under different conditions. (**C**) Yeast cells were transformed with plasmids constitutively expressing mGold or mVenus and attached to a glass-bottom plate. Several thousand cells were photobleached using continuous widefield 508/25-nm illumination at 20 mW/mm^2 for 420 s. Yellow fluorescence images were taken every 10 s during photobleaching.

The fluorescence intensity was normalized to the initial fluorescence (F/F_0). Data points correspond to mean values (n = 3 independent cultures). For each culture, photobleaching curves were obtained for > 500 cells and averaged. The shaded areas represent the SEM but are too small to be visible on the graph. The area under the curve for each sample was computed and the unpaired two-tailed t test was conducted. $p \leq 0.0001$. (**D**) Human cells (HEK239A) were transiently transfected with plasmids constitutively expressing mGold or mVenus and attached to a glass bottom plate. Several hundred cells were photobleached using continuous widefield 508/25-nm illumination at 20 mW/mm^2 for 420 s. Yellow fluorescence images were taken every 10 s during photobleaching. The fluorescence intensity was normalized to the initial fluorescence (F/F_0). Data points correspond to mean values (n = 3 independent transfections). The mean values of 3 independent transfections are shown. The shaded areas represent the SEM but are too small to be visible on the graph. The area under the curve for each sample was computed and an unpaired two-tailed test was conducted. $p \leq 0.0001$. (**E**) Human cells (HEK239A) cells were prepared as described in (D). Cells expressing mGold or mVenus were continuously photobleached and imaged using a laser scanning confocal microscope. A 514-nm laser at 32 µW was used. The data points correspond to the mean of 17 (mVenus) or 15 (mGold) cells. The shaded areas represent the SEM but may be too small to be visible on the graph. The area under the curve for each sample was computed and an unpaired two-tailed t-test was conducted. $p \leq 0.0001$.

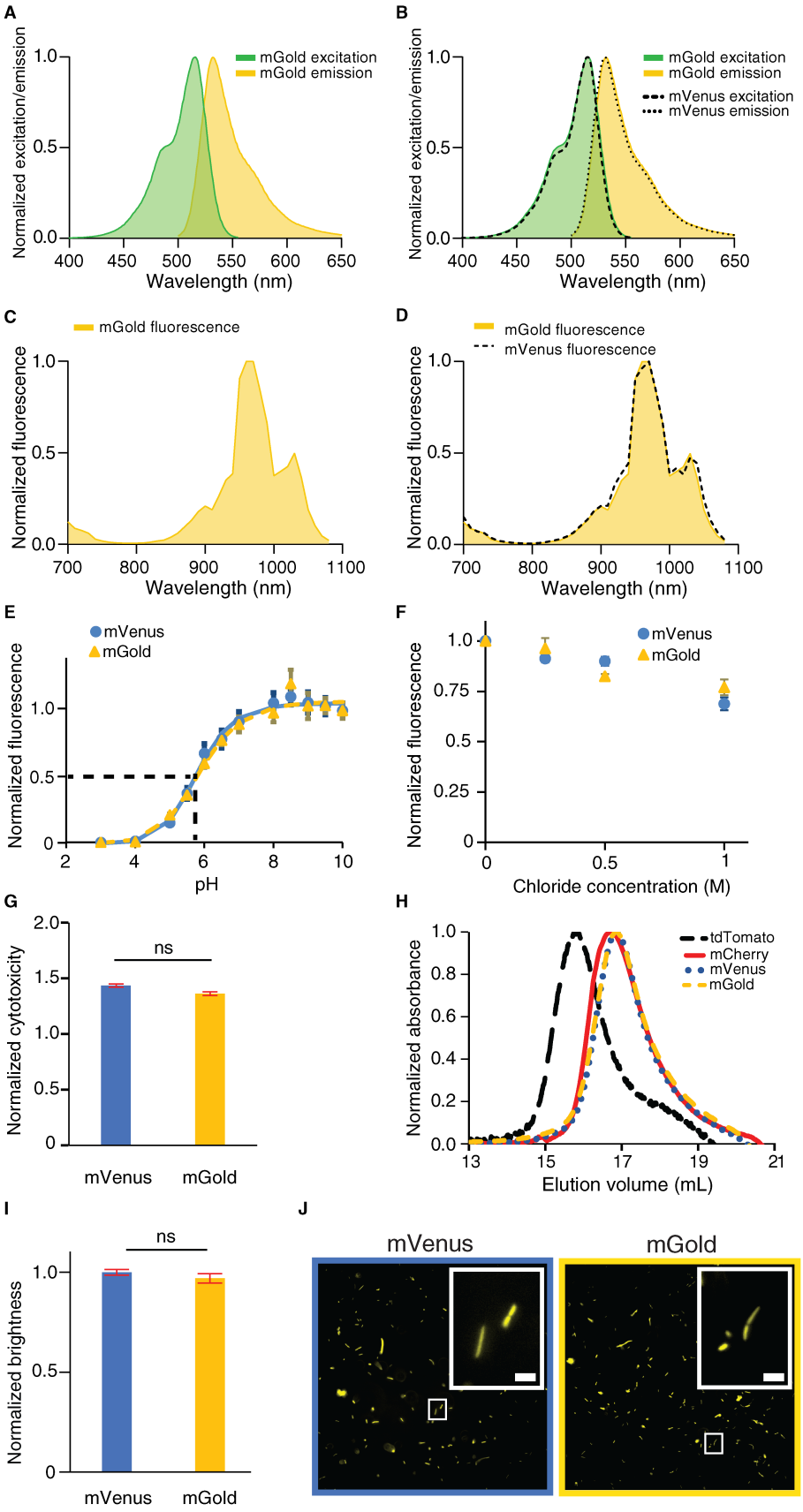
A
Normalized excitation/emission
1.0
0.5
0.0
400
450
500
550
600
650
Wavelength (nm)
mGold excitation
mGold emission
B
Normalized excitation/emission
mGold excitation
mGold emission
mVenus excitation
mVenus emission
Wavelength (nm)
C
Normalized fluorescence
mGold fluorescence
700
800
900
1000
1100
Wavelength (nm)
D
Normalized fluorescence
mGold fluorescence
mVenus fluorescence
Wavelength (nm)
E
Normalized fluorescence
mVenus
mGold
2
4
6
8
10
pH
F
Normalized fluorescence
mVenus
mGold
0.75
0.25
0
0.5
1
Chloride concentration (M)
G
Normalized cytotoxicity
2.0
1.5
ns
mVenus
mGold
H
Normalized absorbance
tdTomato
mCherry
mVenus
mGold
13
15
17
19
21
Elution volume (mL)
I
Normalized brightness
ns
mVenus
mGold
J
mVenus
mGold

Fig. S8. Characterization of mGold photophysical properties. (A-D) The one-photon and two-photon spectra of mGold are similar to those of mVenus. (**A**) Excitation (green) and emission (yellow) spectra of a solution of purified mGold proteins. The spectra for 9 technical replicates were obtained, normalized to their respective maxima, and averaged. (**B**) The mGold spectra in (A) overlaid with the excitation (dashed line) and emission (dotted line) spectra of a solution of purified mVenus proteins. 7 technical replicates were measured for mVenus and averaged as for mGold. (**C**,**D**) Two-photon excitation spectra of (C) mGold and (D) mGold overlaid with that of mVenus (dashed line). Both YFPs were expressed in HEK239A cells. Each spectrum was normalized to its peak fluorescence. Traces show the mean of $n > 20$ cells. The two-photon laser was not compensated for dispersion. (**E**) pH titration of mGold and mVenus. Fluorescence of purified mGold or mVenus suspended in solutions with various pH levels was measured. Fluorescence values were normalized to that at pH 10.0 and the mean of 4 technical replicates are shown. The lines represent the best fit of sigmoidal curves. The error bars indicate SEM. (**F**) mGold and mVenus are similarly insensitive to chloride. The fluorescence of purified mGold or mVenus suspended in buffers with different chloride concentrations was measured. Fluorescence values were normalized to those obtained in a solution without chloride and the mean of 4 technical replicates are shown. The error bars indicate SEM. (**G**) mGold and mVenus have similar profiles of low cytotoxicity. Cytotoxicity values were calculated as described in the Methods and normalized to those of EGFP. The mean values of $n = 3$ independent transfections are shown. The error bars indicate SEM. The Mann-Whitney U test was used for statistical analysis. 'ns' = not significant. (**H**) Size exclusion chromatography demonstrates that mGold is a monomer at 10 μM *in vitro*. tdTomato (tandem dimer), mCherry (monomer), and mVenus (monomer) were used as size standards. Each fluorescent protein was at 10 μM (6.5 μM for tdTomato) and was run separately. mVenus and mGold were detected by measuring the absorbance at 515 nm. tdTomato and mCherry were detected by measuring the absorbance at 555 nm and 587 nm, respectively. Absorbance values were normalized to the maximum absorbance. (**I, J**) Bacterial cells were transformed with mVenus or mGold expression plasmids. FP expression was induced using 1 mM IPTG and the cells were imaged at mid-log phase (OD_{600} ~ 0.3) using a 40X objective and 508/25-nm illumination. (**I**) mGold has a similar brightness as mVenus in bacteria. For each FP, the brightness of 100-200 cells was determined and the mean yellow fluorescence was determined and normalized to that of mVenus. The data plotted correspond to mean values ($n = 3$ independent cultures). The error bars represent the SEM. An unpaired two-tailed t test was conducted. 'ns' = not significant. (**J**) Representative images of mVenus and mGold expressed in bacteria. Scale bars, 5 μm. Inset, magnified region of the white rectangle.

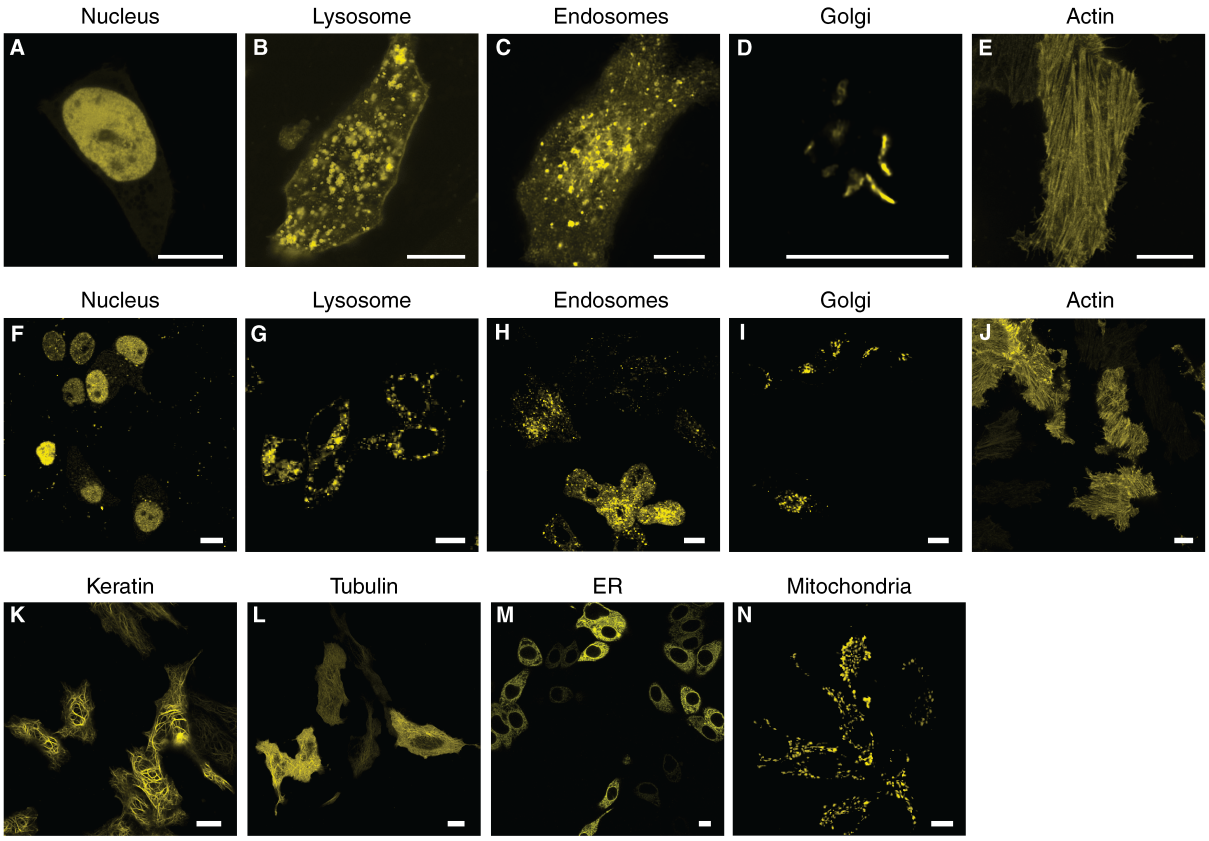

Fig. S9. Confocal images of HeLa cells expressing mGold fused to subcellular localization tags. (**A-E**) For each construct, we indicate the name of mGold's fusion partner, the position of the tag (N- or C-terminal with respect to the fluorescent protein), and the number of residues in the linker between the two proteins. Scale bars, 10 μm. (**A**) mGold-Chaf1a-C-10 (Nucleus) (**B**) mGold-Lamp1-N-20 (Lysosome) (**C**) mGold-RAB4A-C-7 (Endosome) (**D**) mGold-Man2a1-N-10 (Golgi apparatus) (**E**) mGold-ACTB-C-18 (Cytoskeleton, actin). (**F-J**) Zoomed out images of cells expressing the constructs mentioned in A to E. Scale bars, 10 μm. (**K-N**) Zoomed out images of cells expressing the constructs mentioned in Fig. 5D. Scale bars, 10 μm.

Protein	λ_{ex}	λ_{em}	ε	Ψ	Molecular Brightness	pKa	K_d for Cl^- (M)	Photobleaching Half-Life (s)
mGold	515	531	107 ± 6	0.64	68	5.9	> 1	29.8 ± 0.1
mVenus	515	532	110 ± 6	0.65	72	5.9	> 1	10.1 ± 0.2

Table S1. Characterization of mGold's photophysical properties using purified proteins.

λ_{ex} = Excitation maximum (in nm). λ_{em} = Emission maximum (in nm). ε = Extinction coefficient, in $mM^{-1}cm^{-1}$; SEM is shown (n = 3 technical replicates). Ψ = Quantum yield of fluorescence. Molecular brightness was calculated as a product of ε and Ψ. pKa was calculated as the pH at which the *in vitro* fluorescence intensity is half of its maximal value (SEM for n = 3 technical replicates was < 0.1). K_d for Cl^- was calculated as the concentration of Cl^- which fluorescence intensity to reach half its initial value. Both mGold and mVenus retained more than half their initial fluorescences at 1 M of Cl^-. Photobleaching half-life was determined as the time taken for fluorescence intensity to reach half of its initial value with continuous widefield illumination with 510/25-nm light at 62.5 mW/mm^2. Mean ± SEM is shown. n = 7 technical replicates. Note that the improvement in photostability of mGold compared with mVenus differs from the majority of observations in cells (Fig. 5B), possibly due to differences in preparation or irradiance (*35*).

Supplementary video 1

Visualization of cell division using mGold. HeLa cells co-transfected with mGold-keratin and EBFP2-H2B were imaged every 3 min for 24 hrs. Cells were grown in culture media at 37 °C in air with 5% CO_2 and humidity control. Images were acquired with a 50 ms exposure time using 520-nm excitation light at 24.4 mW/mm^2 for YFP and 405-nm light at 1.1 mW/mm^2 for BFP. The video was compiled at 25 frames per second. Scale bar, 20 μm.

Supplementary video 2

Visualization of cell attachment using mGold. HeLa cells co-transfected with mGold-keratin and EBFP2-H2B were imaged every 30 s for 6 hrs. Cells were grown in culture media at 37 °C in air with 5% CO_2 and humidity control. Images were acquired with a 50 ms exposure time using 520-nm excitation light at 54.5 mW/mm^2 for YFP and 405-nm light at 1.1 mW/mm^2 for BFP. The white arrow in the first frame points to the cell that will attach to the glass substrate. The video was compiled at 25 frames per second. Scale bar, 20 μm.

REFERENCES AND NOTES

1. J. Shendure, G. M. Findlay, M. W. Snyder, Genomic medicine–progress, pitfalls, and promise. *Cell* **177**, 45–57 (2019).

2. P. A. G. Tizei, E. Csibra, L. Torres, V. B. Pinheiro, Selection platforms for directed evolution in synthetic biology. *Biochem. Soc. Trans.* **44**, 1165–1175 (2016).

3. N. Nitta, T. Sugimura, A. Isozaki, H. Mikami, K. Hiraki, S. Sakuma, T. Iino, F. Arai, T. Endo, Y. Fujiwaki, H. Fukuzawa, M. Hase, T. Hayakawa, K. Hiramatsu, Y. Hoshino, M. Inaba, T. Ito, H. Karakawa, Y. Kasai, K. Koizumi, S. W. Lee, C. Lei, M. Li, T. Maeno, S. Matsusaka, D. Murakami, A. Nakagawa, Y. Oguchi, M. Oikawa, T. Ota, K. Shiba, H. Shintaku, Y. Shirasaki, K. Suga, Y. Suzuki, N. Suzuki, Y. Tanaka, H. Tezuka, C. Toyokawa, Y. Yalikun, M. Yamada, M. Yamagishi, T. Yamano, A. Yasumoto, Y. Yatomi, M. Yazawa, D. D. Carlo, Y. Hosokawa, S. Uemura, Y. Ozeki, K. Goda, Intelligent Image-Activated Cell Sorting. *Cell* **175**, 266–276.e13 (2018).

4. N. Rimon, M. Schuldiner, Getting the whole picture: Combining throughput with content in microscopy. *J. Cell Sci.* **124**, 3743–3751 (2011).

5. M. Boutros, F. Heigwer, C. Laufer, Microscopy-based high-content screening. *Cell* **163**, 1314–1325 (2015).

6. G. Emanuel, J. R. Moffitt, X. Zhuang, High-throughput, image-based screening of pooled genetic-variant libraries. *Nat. Methods* **14**, 1159–1162 (2017).

7. D. Feldman, A. Singh, J. L. Schmid-Burgk, R. J. Carlson, A. Mezger, A. J. Garrity, F. Zhang, P. C. Blainey, Optical pooled screens in human cells. *Cell* **179**, 787–799.e17 (2019).

8. K. D. Piatkevich, E. E. Jung, C. Straub, C. Linghu, D. Park, H.-J. Suk, D. R. Hochbaum, D. Goodwin, E. Pnevmatikakis, N. Pak, T. Kawashima, C.-T. Yang, J. L. Rhoades, O. Shemesh, S. Asano, Y.-G. Yoon, L. Freifeld, J. L. Saulnier, C. Riegler, F. Engert, T. Hughes, M. Drobizhev, B. Szabo, M. B. Ahrens, S. W. Flavell, B. L. Sabatini, E. S. Boyden, A robotic multidimensional directed evolution approach applied to fluorescent voltage reporters. *Nat. Chem. Biol.* **14**, 352–360 (2018).

9. B. Chen, S. Lim, A. Kannan, S. C. Alford, F. Sunden, D. Herschlag, I. K. Dimov, T. M. Baer, J. R. Cochran, High-throughput analysis and protein engineering using microcapillary arrays. *Nat. Chem. Biol.* **12**, 76–81 (2016).

10. S. Luro, L. Potvin-Trottier, B. Okumus, J. Paulsson, Isolating live cells after high-throughput, long-term, time-lapse microscopy. *Nat. Methods* **17**, 93–100 (2020).

11. J. R. Kovac, J. Voldman, Intuitive, image-based cell sorting using optofluidic cell sorting. *Anal. Chem.* **79**, 9321–9330 (2007).

12. L. Binan, J. Mazzaferri, K. Choquet, L.-E. Lorenzo, Y. C. Wang, E. B. Affar, Y. De Koninck, J. Ragoussis, C. L. Kleinman, S. Costantino, Live single-cell laser tag. *Nat. Commun.* **7**, 11636 (2016).

13. L. Binan, F. Bélanger, M. Uriarte, J. F. Lemay, J. C. Pelletier de Koninck, J. Roy, E. B. Affar, E. Drobetsky, H. Wurtele, S. Costantino, Opto-magnetic capture of individual cells based on visual phenotypes. *eLife* **8**, (2019).

14. M.-P. Chien, C. A. Werley, S. L. Farhi, A. E. Cohen, Photostick: A method for selective isolation of target cells from culture. *Chem. Sci.* **6**, 1701–1705 (2015).

15. X. X. Zhou, M. Z. Lin, Photoswitchable fluorescent proteins: Ten years of colorful chemistry and exciting applications. *Curr. Opin. Chem. Biol.* **17**, 682–690 (2013).

16. K. A. Lukyanov, D. M. Chudakov, S. Lukyanov, V. V. Verkhusha, Innovation: Photoactivatable fluorescent proteins. *Nat. Rev. Mol. Cell Biol.* **6**, 885–891 (2005).

17. G. D. Victora, T. A. Schwickert, D. R. Fooksman, A. O. Kamphorst, M. Meyer-Hermann, M. L. Dustin, M. C. Nussenzweig, Germinal center dynamics revealed by multiphoton microscopy with a photoactivatable fluorescent reporter. *Cell* **143**, 592–605 (2010).

18. C. Medaglia, A. Giladi, L. Stoler-Barak, M. De Giovanni, T. M. Salame, A. Biram, E. David, H. Li, M. Iannacone, Z. Shulman, I. Amit, Spatial reconstruction of immune niches by combining photoactivatable reporters and scRNA-seq. *Science* **358**, 1622–1626 (2017).

19. M. Tomura, N. Yoshida, J. Tanaka, S. Karasawa, Y. Miwa, A. Miyawaki, O. Kanagawa, Monitoring cellular movement *in vivo* with photoconvertible fluorescence protein "Kaede" transgenic mice. *Proc. Natl. Acad. Sci. U.S.A.* **105**, 10871–10876 (2008).

20. G. H. Patterson, J. Lippincott-Schwartz, A photoactivatable GFP for selective photolabeling of proteins and cells. *Science* **297**, 1873–1877 (2002).

21. E. A. Specht, E. Braselmann, A. E. Palmer, A critical and comparative review of fluorescent tools for live-cell imaging. *Annu. Rev. Physiol.* **79**, 93–117 (2017).

22. F. V. Subach, G. H. Patterson, S. Manley, J. M. Gillette, J. Lippincott-Schwartz, V. V. Verkhusha, Photoactivatable mCherry for high-resolution two-color fluorescence microscopy. *Nat. Methods* **6**, 153–159 (2009).

23. F. Helmchen, W. Denk, Deep tissue two-photon microscopy. *Nat. Methods* **2**, 932–940 (2005).

24. J. B. Grimm, B. P. English, H. Choi, A. K. Muthusamy, B. P. Mehl, P. Dong, T. A. Brown, J. Lippincott-Schwartz, Z. Liu, T. Lionnet, L. D. Lavis, Bright photoactivatable fluorophores for single-molecule imaging. *Nat. Methods* **13**, 985–988 (2016).

25. H. H. Yang, F. St-Pierre, Genetically encoded voltage indicators: Opportunities and challenges. *J. Neurosci.* **36**, 9977–9989 (2016).

26. A. V. Mamontova, A. P. Grigoryev, A. S. Tsarkova, K. A. Lukyanov, A. M. Bogdanov, Struggle for photostability: Bleaching mechanisms of fluorescent proteins. *Russ. J. Bioorg. Chem.* **43**, 625–633 (2017).

27. G.-J. Kremers, J. Goedhart, E. B. van Munster, T. W. J. Gadella, Cyan and yellow super fluorescent proteins with improved brightness, protein folding, and FRET Förster radius. *Biochemistry* **45**, 6570–6580 (2006).

28. E. Balleza, J. M. Kim, P. Cluzel, Systematic characterization of maturation time of fluorescent proteins in living cells. *Nat. Methods* **15**, 47–51 (2018).

29. Z. Padamsey, A. Jeans, Imaging synaptic vesicles using VGLUT1-venus knock-in mice: Insights into the dynamic nature of intersynaptic vesicle exchange. *J. Neurosci.* **32**, 3284–3286 (2012).

30. S. Shibata, A. Yasuda, F. Renault-Mihara, S. Suyama, H. Katoh, T. Inoue, Y. U. Inoue, N. Nagoshi, M. Sato, M. Nakamura, C. Akazawa, H. Okano, *Sox10*-Venus mice: A new tool for real-time labeling of neural crest lineage cells and oligodendrocytes. *Mol. Brain* **3**, 31 (2010).

31. A. Larrieu, A. Champion, J. Legrand, J. Lavenus, D. Mast, G. Brunoud, J. Oh, S. Guyomarc'h, M. Pizot, E. E. Farmer, C. Turnbull, T. Vernoux, M. J. Bennett, L. Laplaze, A fluorescent hormone biosensor reveals the dynamics of jasmonate signalling in plants. *Nat. Commun.* **6**, 6043 (2015).

32. J. S. Marvin, B. Scholl, D. E. Wilson, K. Podgorski, A. Kazemipour, J. A. Müller, S. Schoch, F. J. U. Quiroz, N. Rebola, H. Bao, J. P. Little, A. N. Tkachuk, E. Cai, A. W. Hantman, S. S.-H. Wang, V. J. DePiero, B. G. Borghuis, E. R. Chapman, D. Dietrich, D. A. DiGregorio, D. Fitzpatrick, L. L. Looger, Stability, affinity, and chromatic variants of the glutamate sensor iGluSnFR. *Nat. Methods.* 15, 936–939 (2018).

33. N. C. Shaner, M. Z. Lin, M. R. McKeown, P. A. Steinbach, K. L. Hazelwood, M. W. Davidson, R. Y. Tsien, Improving the photostability of bright monomeric orange and red fluorescent proteins. *Nat. Methods* **5**, 545–551 (2008).

34. K. M. Dean, J. L. Lubbeck, L. M. Davis, C. K. Regmi, P. P. Chapagain, B. S. Gerstman, R. Jimenez, A. E. Palmer, Microfluidics-based selection of red-fluorescent proteins with decreased rates of photobleaching. *Integr. Biol.* **7**, 263–273 (2015).

35. P. J. Cranfill, B. R. Sell, M. A. Baird, J. R. Allen, Z. Lavagnino, H. M. de Gruiter, G.-J. Kremers, M. W. Davidson, A. Ustione, D. W. Piston, Quantitative assessment of fluorescent proteins. *Nat. Methods* **13**, 557–562 (2016).

36. K. M. Dean, J. L. Lubbeck, J. K. Binder, L. R. Schwall, R. Jimenez, A. E. Palmer, Analysis of red-fluorescent proteins provides insight into dark-state conversion and photodegradation. *Biophys. J.* **101**, 961–969 (2011).

37. A. A. Tokmakov, A. Kurotani, T. Takagi, M. Toyama, M. Shirouzu, Y. Fukami, S. Yokoyama, Multiple post-translational modifications affect heterologous protein synthesis. *J. Biol. Chem.* **287**, 27106–27116 (2012).

38. Y. Nov, When second best is good enough: Another probabilistic look at saturation mutagenesis. *Appl. Environ. Microbiol.* **78**, 258–262 (2012).

39. L. Chappell, A. J. C. Russell, T. Voet, Single-Cell (Multi)omics Technologies. *Annu. Rev. Genomics Hum. Genet.* 19, 15–41 (2018).

40. A. V. Dubois, P. Midoux, D. Gras, M. Si-Tahar, D. Bréa, S. Attucci, M.-K. Khelloufi, R. Ramphal, P. Diot, F. Gauthier, V. Hervé, Poly-L-Lysine compacts DNA, kills bacteria, and improves protease inhibition in cystic fibrosis sputum. *Am. J. Respir. Crit. Care Med.* **188**, 703–709 (2013).

41. T. M. P. Hartwich, F. V. Subach, L. Cooley, V. V. Verkhusha, J. Bewersdorf, Determination of two-photon photoactivation rates of fluorescent proteins. *Phys. Chem. Chem. Phys.* **15**, 14868–14872 (2013).

42. P. Rompolas, K. R. Mesa, K. Kawaguchi, S. Park, D. Gonzalez, S. Brown, J. Boucher, A. M. Klein, V. Greco, Spatiotemporal coordination of stem cell commitment during epidermal homeostasis. *Science* **352**, 1471–1474 (2016).

43. N. Hasle, A. Cooke, S. Srivatsan, H. Huang, J. J. Stephany, Z. Krieger, D. Jackson, W. Tang, S. Pendyala, R. J. Monnat Jr., C. Trapnell, E. M. Hatch, D. M. Fowler, High-throughput, microscope-based sorting to dissect cellular heterogeneity. *Mol. Syst. Biol.* **16**, e9442 (2020).

44. J. R. Enterina, L. Wu, R. E. Campbell, Emerging fluorescent protein technologies. *Curr. Opin. Chem. Biol.* **27**, 10–17 (2015).

45. A. Germond, H. Fujita, T. Ichimura, T. M. Watanabe, Design and development of genetically encoded fluorescent sensors to monitor intracellular chemical and physical parameters. *Biophys. Rev.* **8**, 121–138 (2016).

46. L. Sansalone, S. Tang, J. Garcia-Amorós, Y. Zhang, S. Nonell, J. D. Baker, B. Captain, F. M. Raymo, A photoactivatable far-red/near-infrared BODIPY to monitor cellular dynamics in vivo. *ACS Sens.* **3**, 1347–1353 (2018).

47. K. D. Piatkevich, F. V. Subach, V. V. Verkhusha, Far-red light photoactivatable near-infrared fluorescent proteins engineered from a bacterial phytochrome. *Nat. Commun.* **4**, 2153 (2013).

48. T. Nagai, K. Ibata, E. S. Park, M. Kubota, K. Mikoshiba, A. Miyawaki, A variant of yellow fluorescent protein with fast and efficient maturation for cell-biological applications. *Nat. Biotechnol.* **20**, 87–90 (2002).

49. B. T. Bajar, E. S. Wang, S. Zhang, M. Z. Lin, J. Chu, A guide to fluorescent protein FRET pairs. *Sensors* **16**, 1488 (2016).

50. A. J. Lam, F. St-Pierre, Y. Gong, J. D. Marshall, P. J. Cranfill, M. A. Baird, M. R. McKeown, J. Wiedenmann, M. W. Davidson, M. J. Schnitzer, R. Y. Tsien, M. Z. Lin, Improving FRET dynamic range with bright green and red fluorescent proteins. *Nat. Methods* **9**, 1005–1012 (2012).

51. M. E. Lee, W. C. DeLoache, B. Cervantes, J. E. Dueber, A highly characterized yeast toolkit for modular, multipart assembly. *ACS Synth. Biol.* **4**, 975–986 (2015).

52. A. Meyer, S. Eskandari, S. Grallath, D. Rentsch, AtGAT1, a high affinity transporter for γ-aminobutyric acid in *Arabidopsis thaliana*. *J. Biol. Chem.* **281**, 7197–7204 (2006).

53. D. B. Flagfeldt, V. Siewers, L. Huang, J. Nielsen, Characterization of chromosomal integration sites for heterologous gene expression in *Saccharomyces cerevisiae*. *Yeast* **26**, 545–551 (2009).

54. B. T. Bajar, E. S. Wang, A. J. Lam, B. B. Kim, C. L. Jacobs, E. S. Howe, M. W. Davidson, M. Z. Lin, J. Chu, Improving brightness and photostability of green and red fluorescent proteins for live cell imaging and FRET reporting. *Sci. Rep.* **6**, 20889 (2016).

55. F. St-Pierre, J. D. Marshall, Y. Yang, Y. Gong, M. J. Schnitzer, M. Z. Lin, High-fidelity optical reporting of neuronal electrical activity with an ultrafast fluorescent voltage sensor. *Nat. Neurosci.* **17**, 884–889 (2014).

56. S. Chamberland, H. H. Yang, M. M. Pan, S. W. Evans, S. Guan, M. Chavarha, Y. Yang, C. Salesse, H. Wu, J. C. Wu, T. R. Clandinin, K. Toth, M. Z. Lin, F. St-Pierre, Fast two-photon imaging of subcellular voltage dynamics in neuronal tissue with genetically encoded indicators. *eLife* **6**, e25690 (2017).

57. A. W. Nguyen, P. S. Daugherty, Evolutionary optimization of fluorescent proteins for intracellular FRET. *Nat. Biotechnol.* **23**, 355–360 (2005).

58. A. L. Chang-Graham, H. A. Danhof, M. A. Engevik, C. Tomaro-Duchesneau, U. C. Karandikar, M. K. Estes, J. Versalovic, R. A. Britton, J. M. Hyser, Human intestinal enteroids with inducible neurogenin-3 expression as a novel model of gut hormone secretion. *Cell. Mol. Gastroenterol. Hepatol.* **8**, 209–229 (2019).

59. R. D. Gietz, R. H. Schiestl, Frozen competent yeast cells that can be transformed with high efficiency using the LiAc/SS carrier DNA/PEG method. *Nat. Protoc.* **2**, 1–4 (2007).

60. S. Berg, D. Kutra, T. Kroeger, C. N. Straehle, B. X. Kausler, C. Haubold, M. Schiegg, J. Ales, T. Beier, M. Rudy, K. Eren, J. I. Cervantes, B. Xu, F. Beuttenmueller, A. Wolny, C. Zhang, U. Koethe, F. A. Hamprecht, A. Kreshuk, ilastik: interactive machine learning for (bio)image analysis. *Nat. Methods* **16**, 1226–1232 (2019).

61. C. T. Rueden, J. Schindelin, M. C. Hiner, B. E. DeZonia, A. E. Walter, E. T. Arena, K. W. Eliceiri, ImageJ2: ImageJ for the next generation of scientific image data. *BMC Bioinformatics* **18**, 529 (2017).

62. H. J. Motulsky, R. E. Brown, Detecting outliers when fitting data with nonlinear regression – a new method based on robust nonlinear regression and the false discovery rate. *BMC Bioinformatics* **7**, 123 (2006).

63. I. I. Shemiakina, G. V. Ermakova, P. J. Cranfill, M. A. Baird, R. A. Evans, E. A. Souslova, D. B. Staroverov, A. Y. Gorokhovatsky, E. V. Putintseva, T. V. Gorodnicheva, T. V. Chepurnykh, L. Strukova, S. Lukyanov, A. G. Zaraisky, M. W. Davidson, D. M. Chudakov, D. Shcherbo, A monomeric red fluorescent protein with low cytotoxicity. *Nat. Commun.* **3**, 1204 (2012).

64. H.-W. Ai, M. A. Baird, Y. Shen, M. W. Davidson, R. E. Campbell, Engineering and characterizing monomeric fluorescent proteins for live-cell imaging applications. *Nat. Protoc.* **9**, 910–928 (2014).

65. A. Ghasemi, S. Zahediasl, Normality tests for statistical analysis: A guide for non-statisticians. *Int. J. Endocrinol. Metab.* **10**, 486–489 (2012).

66. S. Henikoff, J. G. Henikoff, Amino acid substitution matrices from protein blocks. *Proc. Natl. Acad. Sci. U.S.A.* **89**, 10915–10919 (1992).